The International Journal of Advanced Manufacturing Technology (2019) 102:2907–2918
https://doi.org/10.1007/s00170-019-03401-1

ORIGINAL ARTICLE

Effect of microstructure and precipitation phenomena on the mechanical behavior of AA6061-T6 aluminum alloy weld

Maamar Hakem[1,2] · Soltane Lebaili[2] · Stephane Mathieu[3] · Djamel Miroud[2] · Abdelatif Lebaili[2] · Billel Cheniti[1]

Received: 12 October 2018 / Accepted: 29 January 2019 / Published online: 7 February 2019

Abstract

In the present study, the effect of microstructure and precipitation phenomena on the micro hardness, tensile strength, impact toughness, and electrochemical behavior of tungsten inert gas (TIG)-welded AA6061-T6 aluminum alloy are investigated. The microstructure features showed mainly the grains of aluminum solid solution with the presence of some precipitates at the grain boundaries. Scanning electron microscope micrographs exhibited the presence of Fe-based intermetallic and β-equilibrium precipitates throughout α-Al grains. In the heat-affected zone (HAZ), the dissolution, over-aged, and coalescence of precipitates are observed; their hardening effects disappear and a decrease in strength and hardness are noticed. The fracture toughness values of each zone at different temperatures using Charpy V-notch test remained constant where the HAZ presents the highest absorbed energy. However, the temperature did not have a significant effect on the absorbed energy for each zone. In addition, the fractured surface of base metal (BM) and HAZ are characterized by dimple-like structure and they are larger in the HAZ. The electrochemical behavior of each zone of the weld evaluated in NaCl + H_2O_2 solution revealed that the corrosion current density of BM and HAZ is lower than that of molten zone (MZ), which displays high corrosion current density in this electrolyte and would be fastest to corrode.

Keywords Aluminum alloys · TIG welding · Precipitates · Microstructure · Fractography · Electrochemical behavior

1 Introduction

The AA6061-T6 aluminum alloy displays high strength and reasonable weldability. The main alloying chemical elements are magnesium and silicon; they increase the alloy strength through precipitation hardening [1, 2]. This alloy finds various applications due to it higher strength to weight ratio. It is used in fabrication of tank for transporting various liquids, automotive industry, marine frames, and pipeline, where it is often welded during manufacturing process. Several difficulties are encountered during its welding with the use of tungsten inert gas (TIG) process. They are related to its solidification and its high thermal conductivity [3, 4]. However, the heat treatment caused by the welding of this alloy result in significant reduction in hardness and mechanical properties. Since the heat-affected zone (HAZ) undergoes significant cycles of heating and cooling during the welding operation, its properties can significantly change from those of the parent material before

✉ Maamar Hakem
maamarhak@gmail.com

Soltane Lebaili
slebaili@yahoo.fr

Stephane Mathieu
stephane.mathieu@univ-lorraine.fr

Djamel Miroud
dmiroud@usthb.dz

Abdelatif Lebaili
lotfileub@hotmail.fr

Billel Cheniti
cheniti.billel@hotmail.fr

[1] Research Center in Industrial Technologies CRTI, P.O.BOX 64, Cheraga, 16014 Algiers, Algeria

[2] Laboratory of Sciences and Materials Engineering, LSGM, FGMGP, University of Sciences and Technology Houari Boumediene, BP 32, El Alia, Bab Ezzouar, 16111 Algiers, Algeria

[3] Institut Jean Lamour, UMR7198, Université de Lorraine – CNRS, 2 Allée André Guinier-54000, Nancy, France

welding. The effects of the heat generated by welding on the alloy vary with the distance from the weld. It may roughly be divided into areas reflecting the different temperatures reached by the weld piece. The holding time at each temperature is also considered for heat-treatable alloys. To fully anneal these alloys, it is required to hold them at high temperature for several hours. Nevertheless, the heating induced by the welding process generally not fully anneal the HAZ, because of its limited duration, but produce a partial annealing and over-aging conditions. The weldment obtained was generally failed in the area affected by the excessive heat resulting from the welding process [5]. The AA6061 aluminum alloy cannot be welded autogenously or with a filler metal (FM) of the same nuance, without encountering the problem of hot cracking [6]. The employment of an FM of different composition to weld this alloy becomes indispensable. Hence, ER4043 (aluminum-silicon alloy) FM, classified according to the American Welding Society (AWS), is highly recommended for AA6061 aluminum alloy welding due to its well-known solidification-cracking tendency and its microstructure/mechanical properties relationships [7].

The AA6061 welds usually display strong heterogeneity in microstructure and mechanical properties across the different zones. This heterogeneity in mechanical properties results from the inhomogeneous in size, volume fraction, and distribution of the strengthening precipitates in the HAZ [8–10]. Several investigations have been conducted on various aspects of 6xxx heat-treatable welded alloys [5, 11–13].

Many works [14–16] studied the effect of welding process such as TIG, gas metal arc welding (GMAW), and friction stir welding (FSW) on mechanical properties of AA6061. Cabello et al. [17] studied also the microstructure and mechanical properties of FSW- and TIG-welded aluminum alloys and reported that the yield strength of the welded joints decreased compared to those of the base metal (BM). In other research work [18], the mechanical behavior of the AA6061 was investigated and it was noticed that the yield strength decreases when the peak temperature increases and the heating rate decreases which can be explained by precipitates coarsening.

Many other studies have been performed on the corrosion behavior of aluminum alloys, mostly of the 6xxx family welded by different processes [19, 20]. They highlighted the influence of microstructure and precipitation phenomena, essentially the intermetallic particles on the corrosion behavior of these alloys. This behavior can be cathodic or anodic regarding the aluminum matrix. The anodic phase leads to the dissolution of the alloy, whereas a cathodic phase induces the dissolution of the surrounding matrix.

The correlation between the different experimental parameters is of an interest for industrial applications of AA6061 aluminum alloy welds using the ER4043 filler metal, which are relatively scarce in the literature. Therefore, this study aims to evaluate the microstructural aspects of each zone issued from the AA6061 weld joint. The precipitation phenomenon of hardenable phases and its effect on the mechanical properties and the electrochemical behavior of the weldment are particularly studied. Since this alloy is designed to liquefied naturel gas (LNG) pipelines, it is important to consider the toughness at low-temperature conditions. The results of Charpy tests conducted at different temperatures showed that regardless the temperature, the highest absorbed energy is recorded in the HAZ.

2 Materials and methods

In this study, AA6061-T6 aluminum alloy base material pipe of 168.3-mm diameter and 7.11-mm thickness is welded using TIG process with ER4043 as FM. The chemical compositions of the materials used are given in Table 1. 'V' butt joint configuration is prepared to fabricate Multi pass joint (four passes). The welding parameters are presented in Table 2.

Samples are cut perpendicularly to the welding direction, according to the two-interface configuration BM/HAZ/MZ/HAZ/BM, and prepared for optical metallography using standard techniques of mechanical polishing. Final polishing is done using the diamond compound, Alumina (1 μm and 0.3 μm) and standard colloidal silica suspension (OP-U). Afterwards, specimens are chemically etched on the one hand, with Keller's reagent and, on the other hand, anodized with Barker's reagent, in order to reveal the macrostructure and microstructure for a standard bright-field illumination and polarized light techniques, respectively. Microstructural analysis is carried out using light optical microscope (OM) (Universal Microscope UDM-LV100D-U) assisted with an image analyzing software (NIS-Elements D software). Scanning electron microscope (SEM-JEOL JSM-6010 LA) coupled to an energy-dispersive spectroscopy (EDS) for chemical analysis is used to carryout backscattered electrons images (BSE) of ionic polished samples and secondary electrons images (SE) of fractographs issued from Charpy test.

Table 1 Chemical composition of the base material and the filler metal (wt.%)

Elements	Si	Mg	Ti	Cr	Mn	Fe	Cu	Zn	Al
AA 6061-T6	0.7	0.9	0.01	0.05	0.04	0.25	0.29	0.06	Base
ER 4043	5.1	< 0.01	< 0.01	0.01	< 0.01	0.2	0.03	0.01	Base

Table 2 Welding parameters

Alternate TIG Welding	Pass 1	Pass 2	Pass 3	Pass 4
Welding process	TIG			
Current and polarity	AC (−)			
Filler metal	ER 4043			
Filler metal diameter (mm)	2.4			
Current (A)	170	175	175	175
Voltage (V) average	12.70	13.70	13.70	13.70
Welding time (s)	235	240	240	248
Travel speed (mm s^{-1})	2.24	2.20	2.20	2.12
Heat input (kJ mm^{-1})	0.96	1.09	1.09	1.13
Shielding gas	Argon 99.99%			
Flow rate (L min^{-1})	12			

The micro hardness profile across the cross sectional weldment shown in Fig. 1 (dashed line) is conducted using Wilson VH3300 Buehler under 0.2 kgf. The values are obtained from the average of three measurements to check the reproducibility.

Tensile specimens are prepared according to the American Society of Mechanical Engineers (ASME Sec. IX) standard [21] (Fig. 2a) to evaluate the weldment tensile properties. Tensile tests are carried out using 600 KN Satec System Instron USA testing machine. The absorbed energy and fracture behavior are investigated using Hoytom D2-M Charpy test machine with a capacity of 750 J. Reduced Charpy V-notch specimens are machined perpendicular to the weldment, according to the American Standard of Testing Materials (ASTM E23) [22] with the dimensions of (10 mm × 6 mm × 55 mm), notch root radius: 0.25 mm, notch depth: 2 mm, notch and flank angle 45° as illustrated in Fig. 2b. Charpy V-notch specimens are tested in the BM, HAZ and molten zone (MZ) at different temperatures (20 °C, − 30 °C, and − 60 °C) where the fractured surfaces are characterize by SEM.

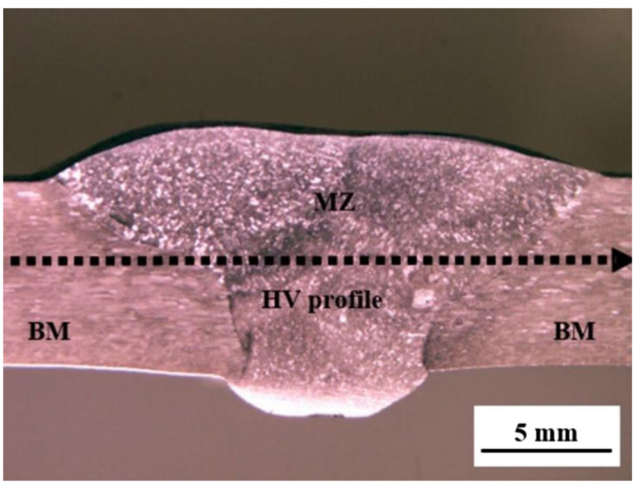

Fig. 1 Macrostructure of the weld joint and schematic illustration of micro hardness profile

The electrochemical measurements are carried out using a Gamry Instrument ZRA.RE/600 potentiostat at room temperature. The potential and polarization test measurements are performed in the BM, HAZ, and MZ. The electrochemical tests are conducted in a flat sample cell with 58.5 g of NaCl + 10 ml of H_2O_2 in 1 l of H_2O (pH 5.9), and a three-electrode fitting in which the working electrode faced the counter electrode (platinum grid). A saturated calomel electrode (SCE) is used as the reference and all potentials are given with respect to SCE. The potentiodynamic scans are recorded with a 0.5 mV s^{-1} scan rate from − 250 mV versus the open circuit potential (E_{oc}) up to a potential such that the current density did not exceed the pre-set value of 20 $mAcm^{-2}$. The open circuit potential (E_{oc}) is recorded just before the polarization measurements. The corrosion current density values (I_{corr}) and the corrosion potential (E_{corr}) are deduced from these polarization measurements.

3 Results and discussion

3.1 Microstructural evolution across the weld joint

Figure 1 illustrates an overview of the weldment macrostructure obtained after welding in four passes. The visual control shows that the welding is homogeneous, without apparent defects. Three regions can be distinguished in the weld joint macrostructure (BM, MZ, and BM) with a symmetrical configuration BM/MZ/BM. The optical micrographs of the microstructure formed in the weld joint after chemical etching are given in Fig. 3a–f. Figure 3a–c show the morphology of the BM, HAZ/MZ interface, and MZ located on the left side of the weld joint. On the other side, using polarized light OM, the microstructures of MZ, MZ/HAZ interface, and BM located on the right side of the weld joint are illustrated in Fig. 3d–f. Furthermore, the use of these two types of optical observation gives complementary information on the textures formed in the weld joint.

The weldment can be separated into five zones and four interfaces that are symmetric from the weld joint centerline and are as follows:

- The molten zone (MZ), located in the center of the weld joint. In this zone, the melting temperature is reached, and the obtained microstructure depends on the welding conditions particularly the cooling rate. Its chemical composition close to the interface results from the dilution of the BM in the MZ.
- The heat-affected zone (HAZ), located on both sides (left and right) of the MZ. This zone is subjected to high temperature but below the melting point, and its structural changes depend on the thermal cycles.

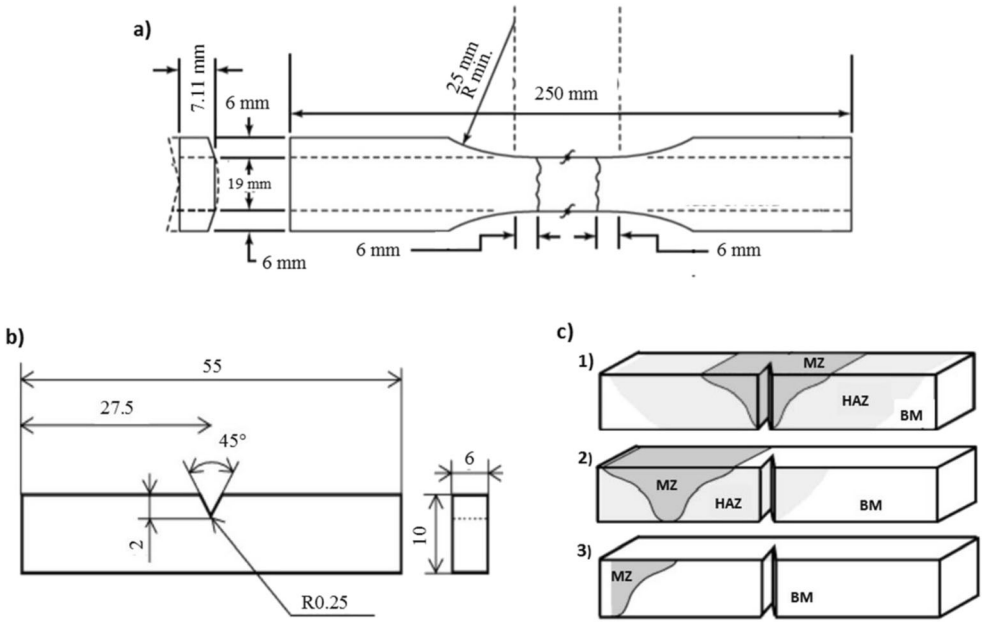

Fig. 2 Geometry of the test specimens. **a** Tensile test specimen [21]. **b** Charpy test specimen [22]. **c** Schematic illustrations of the different positions of the Charpy V-notch

– The base metal (BM), located on both sides (left and right) of the HAZ. The rise in temperature is not sufficient to affect the initial structure in this zone. Therefore, no structural change is noticed.
– The interfaces: BM/HAZ and HAZ/MZ on the left and MZ/HAZ and HAZ/BM on the right side of the weld joint.

The optical micrograph of the BM (Fig. 3a) shows mainly two phases, the α-Al solid solution grains and some precipitates at the grain boundaries. Noting that the AA6061 is a solid phase precipitation-hardening alloy where the α-Al developed under industrial conditions is out of thermodynamic equilibrium and supersaturated with magnesium (Mg) and silicon (Si)

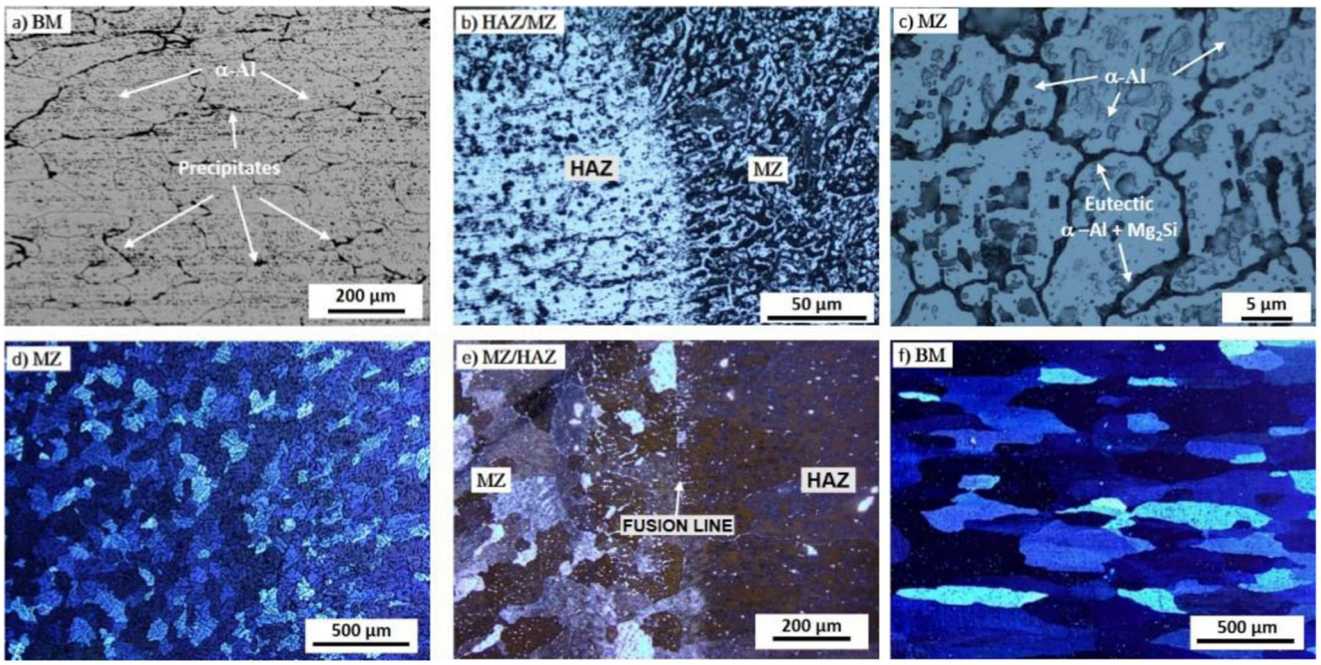

Fig. 3 Optical micrographs of **a**, **f** BM; **b**, **e** HAZ/MZ and MZ/HAZ interfaces; and **c**, **d** MZ

elements. These two elements combined, precipitate in the α-Al matrix during the cooling process and give the precipitates compound.

The BSE-SEM image (Fig. 4a) exhibits the (α-Al) grains with the presence of precipitates of different contrast. White precipitates located at the grain boundaries and dark precipitates which are randomly distributed through the matrix.

The 6xxx series aluminum alloys hardening is obtained by the decomposition in several stages of the supersaturated solid solution resulted from quenching. The precipitation sequence is very complex and depends essentially on the Mg/Si concentration ratio; it takes place in the following stages: α (supersaturated solid solution) → GP zones or clusters of Mg and Si → metastable β″ (coherent) → metastable β′ (semi-coherent) → β stable phase-Mg_2Si (incoherent). The maximum hardening is achieved by the formation of nano-precipitates [23–26], which opposes the dislocations movement during deformation [27, 28]. These sequences are explained in other works using high characterization techniques such as transmission electron microscopy [29, 30].

The EDS analysis of the white precipitates reveals the presence of Fe, Mn, and Cu heavy elements as shown in Fig. 5 and confirms that these precipitates are not the hardening ones. These phases with significant quantities of heavy elements appear brighter than the ones containing light elements. The presence of Fe as an impurity in aluminum AA6061 (Table 1) results in the precipitation of high fraction of coarse Fe- and Si-rich constituents during casting [31, 32]. These large intermetallics (size from 5 to 20 μm) visible in the micrographs showed in Fig. 4a–c, are formed during the elaboration of the material and do not contribute in the alloy hardening [18, 33].

On the other side, the EDS analysis of the dark precipitates reveals the presence of Mg and Si as shown in Fig. 5, which corresponds to the β-equilibrium precipitates. Noting that the fine and coherent hardening β″ precipitates are also present, but due to their nano-size, it is difficult to visualize them (Fig. 4a). These results are in a good agreement with the quasi-binary section of the Al–Mg–Si ternary phase diagram (Fig. 6) [34].

The continuous cooling precipitation of Mg_2Si compound is well detailed in the Al–Mg–Si alloys [35]. During the TIG welding process, high temperature (fusion) is generated in the MZ, and the heat excess is dissipated into the surrounding material, resulting in the formation of the HAZ as shown in Fig. 3b, e. The opposite behavior occurs in the HAZ compared to that during cooling process. Dissolution, over-aged, and coalescence of precipitates are produced (Fig. 4b, c) and their hardening effects

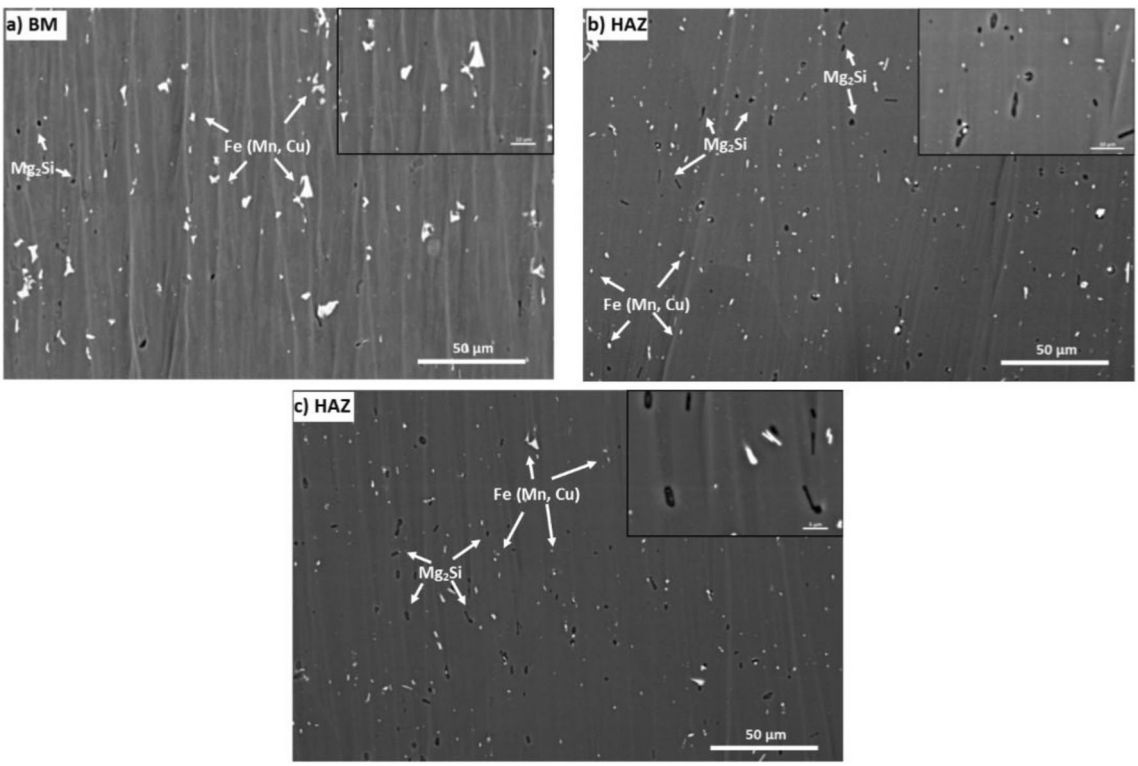

Fig. 4 SEM micrographs of **a** BM, **b** HAZ near the MZ, and **c** HAZ at 20 mm of MZ

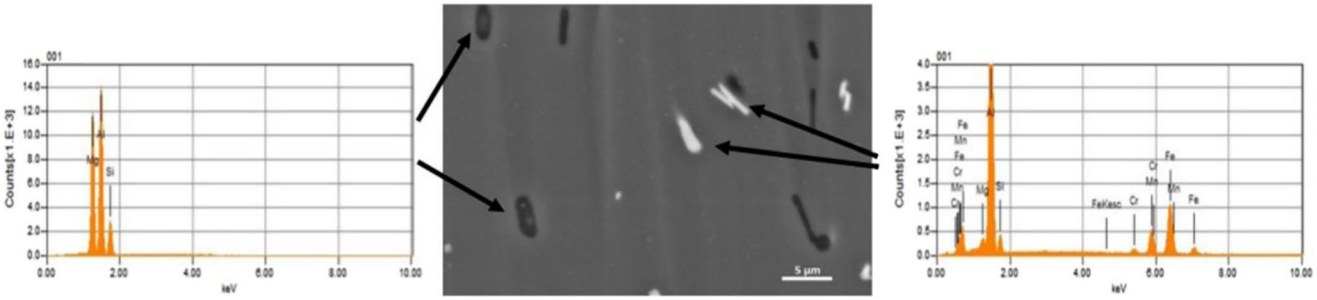

Fig. 5 EDS analysis of dark and white precipitates

disappear, which alters the material's properties of the HAZ. The surface fraction of the white and dark precipitates in each zones is calculated by ImageJ software. Due to the nano-size and the coalescence of the hardening precipitates β″, only 0.1% of dark precipitates (β-Mg_2Si equilibrium precipitates) are visible in the BM (Fig. 4a), and this fraction increases from 0.8% to 1.3% in the HAZ as shown in Fig. 4b, c (depending on the distance from the MZ). No change in white precipitates surface fraction is noticed; this confirms that they do not contribute in the alloy hardening. However, the MZ consists of large grains of (α-Al) and eutectic mixture (Al–Si).

Generally, the MZ is characterized by coarse dendritic grains, interdendritic segregate phases, and the lack of strengthening phases [5, 36]. The total melting of the FM and the partial melting of the BM in the MZ produce two liquids with total miscibility. The obtained liquid contains between 0.7 and 5.1 wt% of Si (see Table 1); it forms therefore a hypoeutectic alloy in accordance with the quasi-binary section of the Al–Mg–Si ternary phase diagram (Fig. 6). During the cooling of this liquid, Mg and Si elements combine with Al to form a quasi-binary α-Al + Mg_2Si eutectic phase with 8.25% Mg and 4.75% Si at the melting point of 595 °C (Fig. 3c). Besides, a few Mg_2Si precipitates is formed near the MZ/BM fusion boundary due to the dilution phenomenon [14, 37, 38]. As illustrated in Table 1, it is clear that the Si element is available in both FM and BM, but the Mg element is only present in the BM. The EDS analysis (Fig. 7) conducted along the fusion boundary confirms the presence of Mg in the MZ as a result from dilution of the BM in the MZ. Figure 7j represents the linear distribution of Mg and Si elements across the interface and confirm the presence of the two elements in both side of fusion boundary.

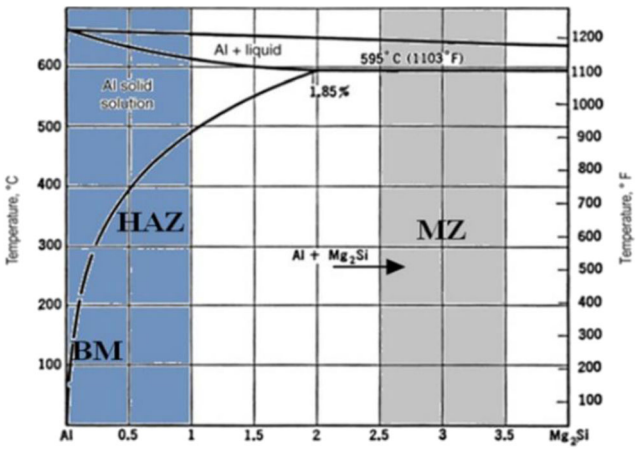

Fig. 6 Quasi-binary section of the Al–Mg–Si ternary phase diagram showing the solid solubility of Mg_2Si in aluminum [34]

3.2 Effect of welding process on the mechanical behavior

Figure 8 illustrates the micro hardness profile according to the BM/HAZ/MZ/HAZ/BM configuration. The profile is practically symmetrical compared to the MZ central axis, which indicates the same mechanical properties of the welded alloy on both sides of this zone. The welding thermal effects on the hardness behavior are therefore reproducible in both sides.

The hardness of the BM is about 105 $HV_{0.2}$ and it varies from 55 $HV_{0.2}$ to 75 $HV_{0.2}$ along the HAZ width (~25 mm). However, the MZ shows the lowest hardness (50~55 $HV_{0.2}$) due to the as-cast nature of the microstructure. Moreover, a small peak of hardness (~60 $HV_{0.2}$) is recorded near the interface in both sides of the MZ. The comparison between these values shows that from BM to the HAZ the hardness decreases by 40% and even more than 50% from BM to MZ. This behavior is directly related to the thermal effect caused by multi-pass (four passes) during welding operation that induces remarkable changes in the microstructure formed in each zone.

The highest hardness of the BM is mainly attributed to the presence of alloying elements (Mg and Si) which undergoes precipitation reaction and form a strengthening nano-precipitates that increase the mechanical properties of the

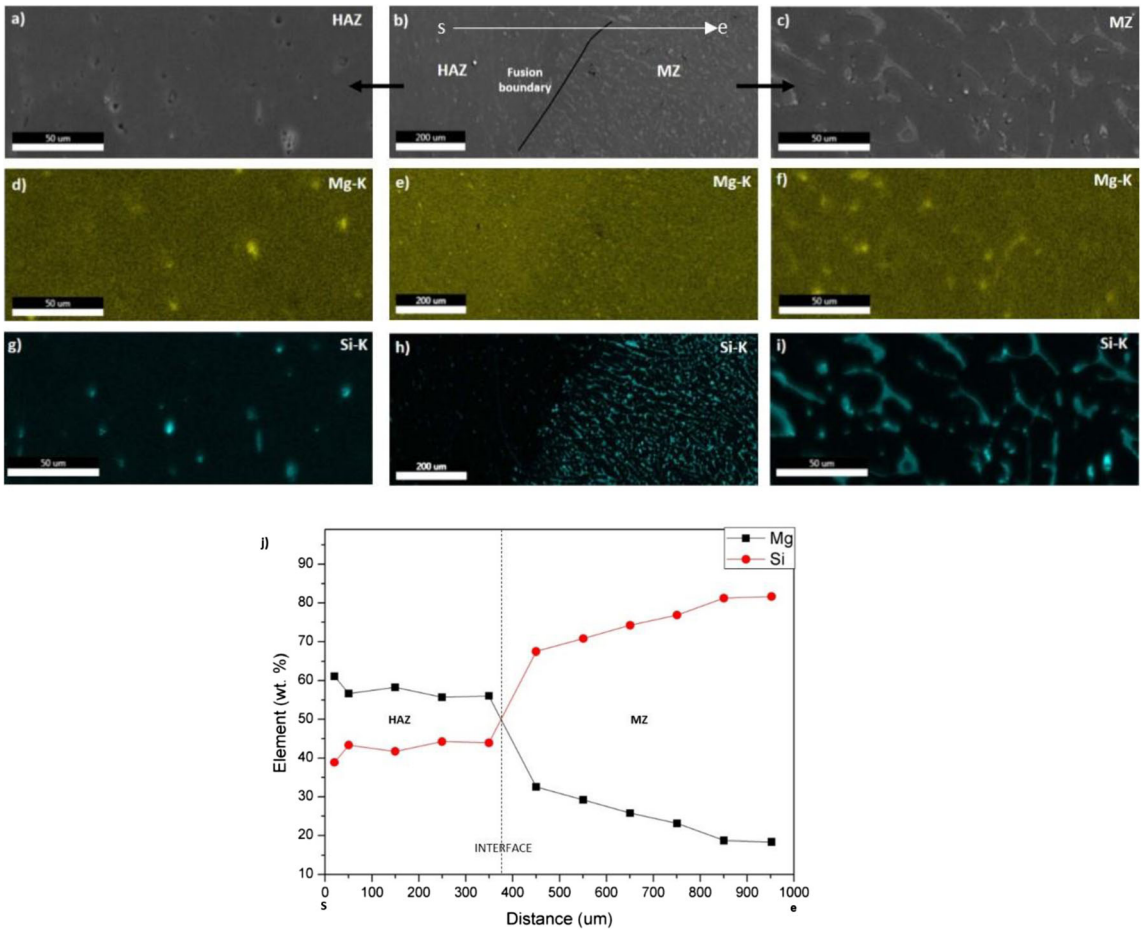

Fig. 7 EDS analysis at the HAZ/MZ interface. **a–c** SEM micrographs. **d–f** Mg mapping distribution. **g–i** Si mapping distribution. **j** Linear analysis of Mg and Si at MZ/HAZ interface

alloy [27, 39]. A drop in hardness already observed in the HAZ is more likely related to microstructural changes (grain coarsening and recrystallization phenomena) and the presence of coalescent precipitates resulting from the thermal cycles generated by welding process [40, 41]. The lowest hardness recorded in the MZ is explained by the coarse and dendritic

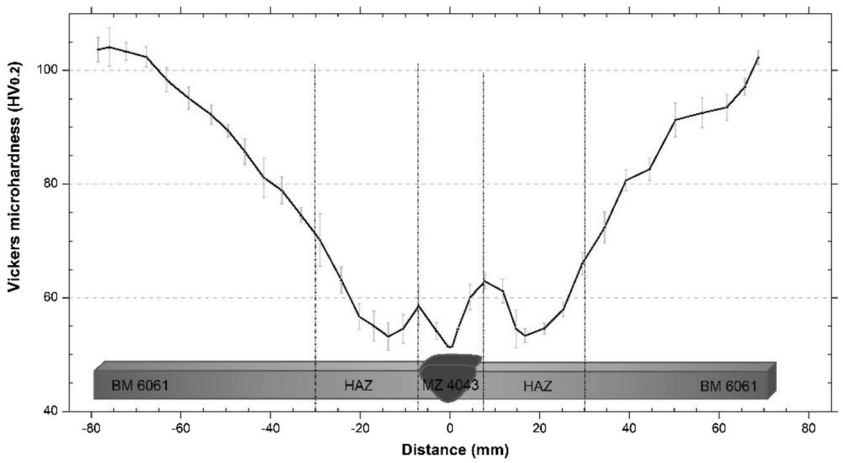

Fig. 8 Vickers micro hardness profile of weldment $HV_{0.2}$

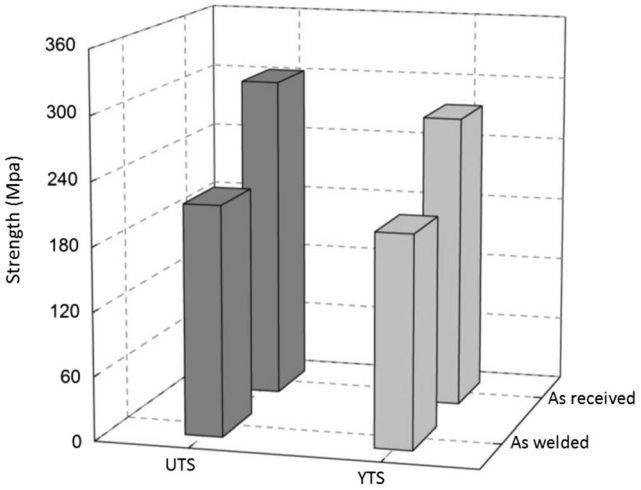

Fig. 9 Histogram of UTS and YTS before and after welding

grain-structure [42]. The peak of hardness (lower than that in BM) observed at MZ/HAZ and HAZ/MZ interfaces close to the fusion boundary is explained by the formation of fine precipitates during cooling or during natural aging.

Figure 9 shows the tensile strength (UTS) and yield strength (YTS) average values of three specimens tested of AA6061-T6 base material and the AA6061-T6 TIG weld joint. As can be seen, the maximum UTS and YTS of the AA6061-T6 base material are 304 MPa and 276 MPa, respectively. However, the UTS and YTS of TIG joint are 216 MPa and 199 MPa, which are, respectively, 29% and 27% lower than the base material ones. The joint efficiency of TIG weld defined as the ratio between tensile strength of welded joint and tensile strength of the base material is 71%. It is noted that, the failure occurred within the HAZ region, where the thermal cycles prevailed leading to the precipitates coalescence.

Figure 10 represents the absorbed energy values of BM, HAZ, and MZ obtained from Charpy test conducted at different temperatures (20 °C, − 30 °C, and − 60 °C). The highest absorbed energy is recorded in HAZ (31 J) and the lowest in MZ (11 J), which are 13% higher and 7% lower than that in the BM (18 J). On the other side, comparing the absorbed energy for each zone at different temperatures, no remarkable variation is noticed.

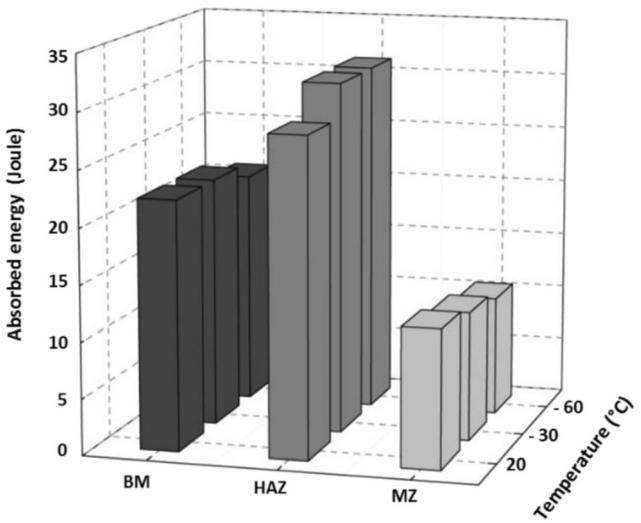

Fig. 10 Absorbed energy at different temperatures for each zone (BM, HAZ, and MZ)

3.3 Fractrographs

Figure 11 shows the fractured surface morphologies of specimens (BM, HAZ, and MZ) issued from Charpy test examined using SEM. The fractured surfaces of each zone are shown for ambient temperature (20 °C) and for low temperature (− 60 °C) and the images are taken at low and high magnifications. Each fractured surface consists of microvoids and dimples indicating ductile fracture mode as shown in Fig. 11a–h. The fractured surfaces of the BM and the HAZ are characterized by dimple-like structure. At the same temperature, the dimples in the HAZ (Fig. 11e–h) are somewhat larger than those in the BM (Fig. 11a–d). The density of the dimples increases with decreasing the temperature indicating a typical ductile fracture mechanism. It is well known that the dimple size exhibits a directly proportional relationship with strength and toughness [43], i.e., the finer the dimples size are, the higher the strength and ductility of the material. Nevertheless, this condition is not the only factor to consider, and a diversity of fracture mechanisms can occur in aluminum alloys due to the microstructure complexity. As mentioned before, the precipitate compounds are uniformly dispersed through the aluminum matrix and grain boundaries, which limit the propagation of micro-cracks during the impact test. Inside the grain, the precipitates act as sites for the formation of voids, which grow and link together to form macro-voids. In Fig. 11b, d, f, h, the apparent bright precipitates particles located in the microvoids show that the void initiation and coalescence take place at the aluminum matrix-precipitates interface. Consequently, the concentration of the stress at the precipitates interface leads to the formation of micro-voids and accelerates crack initiation, further the effect of nano-precipitates β″ must not be ignored. At last, a flat dimple resulting from the as-cast structure is observed in MZ (Fig. 11i–l) and could promote the intergranular fracture.

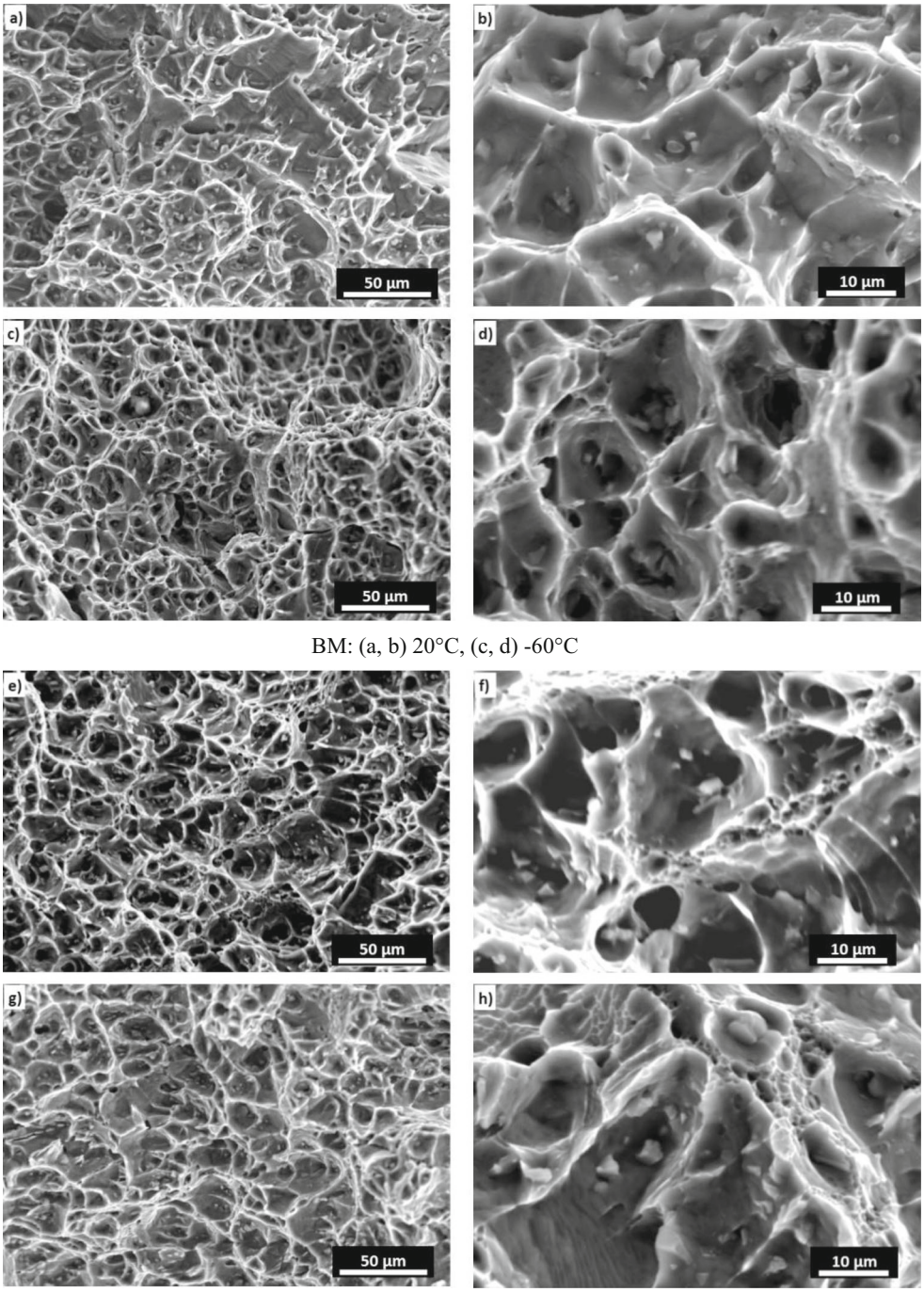

Fig. 11 Fracture surfaces after Charpy impact test. BM: **a**, **b** 20 °C; **c**, **d** − 60 °C. HAZ: **e**, **f** 20 °C; **g**, **h** − 60 °C. MZ: **i**, **j** 20 °C; **k**, **l** − 60 °C

3.4 Electrochemical behavior

The E_{oc} recorded in the solution of 58.5 g of NaCl +10 ml of H_2O_2 in 1 l of H_2O reached a stable value after only 100 s. Thus, the E_{oc} potential has been recorded over 300 s for each zone. The E_{oc} does not significantly differ for the different zones of the weld, especially for the BM and the HAZ. Nevertheless, the MZ (− 698 SCE/mv) shows slightly higher potential (more anodic) than that of the HAZ and BM (− 713 SCE/mv).

Figure 12 shows the polarization curves of the BM, HAZ, and MZ. The $I = f(E)$ curves of BM and HAZ overlap each other. It is clear that the heat treatment engendered by welding

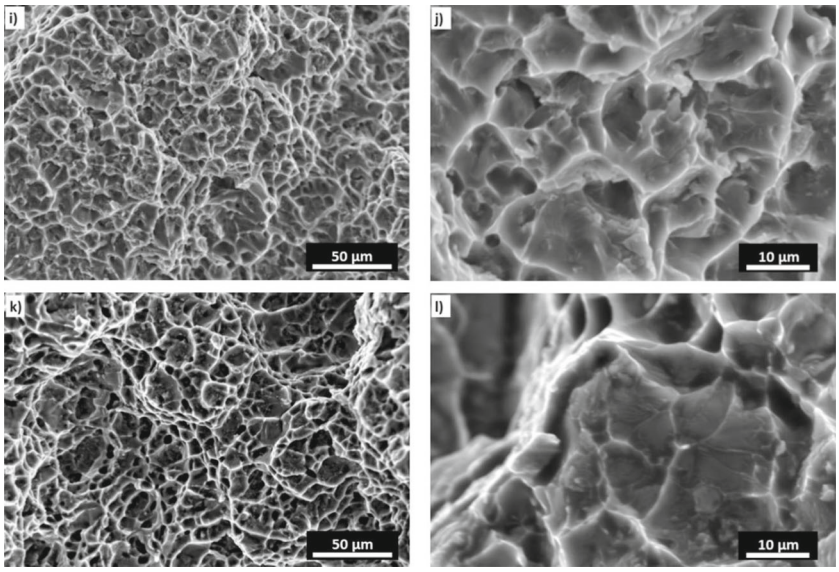

MZ: (i, j) 20°C, (k, l) -60°C

Fig. 11 (continued)

does not significantly affect the electrochemical properties of the specimens. The curves exhibit a cathodic plateau with constant current, which indicates that the corrosion current density is diffusion controlled. The anodic current drastically increased after E_{corr}, showing that, no passivation phenomenon occurs in this electrolyte.

Table 3 summarizes the electrochemical parameters deduced from these experiments. According to the I_{corr} of the MZ (16 µA cm^{-2}) which is higher than that of BM (9 µA cm^{-2}) and HAZ (8.5 µA cm^{-2}), the MZ has the fastest corrosion rate and more susceptible to the corrosion in this electrolyte.

Figure 13a–c presents the SEM micrographs of the different weld zones surfaces after the anodic polarization tests. A localized corrosion aspect of the surface (pitting) is observed. The zones present different pit morphologies, rounded shape in the BM and HAZ zones (see Fig. 13a, b); whereas in MZ (Fig. 13c), the pits do not develop regularly and present right-angled morphologies.

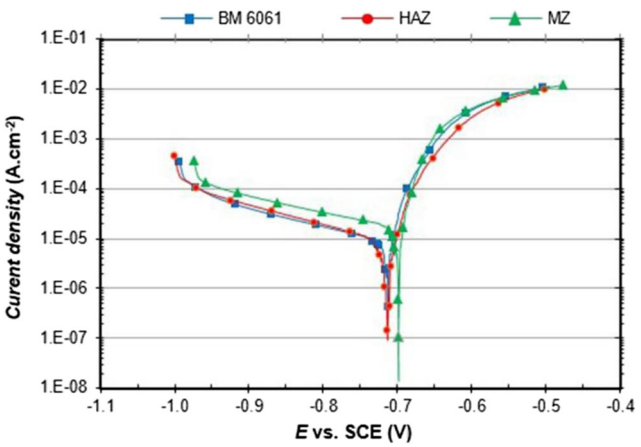

Fig. 12 Polarization curves of the BM, HAZ, and MZ

4 Conclusions

The microstructure, mechanical properties, and fractured surfaces of the AA6061 aluminum alloy-welded joint obtained using TIG welding process are investigated with a focus on the precipitates phenomena and their effect on the hardness and toughness of the weldment. The following main conclusions are obtained:

- The microstructure consist of α-Al solid solution grains and some precipitates at the grain boundaries. The precipitation of β-equilibrium phase throughout the α-Al grains are observed with the presence of Fe-based intermetallic. Moreover, a large α-Al grains and Al–Si eutectic mixture are observed in the MZ with the presence of fine precipitates near the fusion boundary resulting from dilution phenomenon.
- The maximum strength of 216 MPa is obtained, which is 71% of the AA6061-T6 base material.

Table 3 Electrochemical parameters deduced from I = f (E)

	I_{corr}/µA cm^{-2}	E_{corr} vs. SCE/mv	β_a/mV	β_c/mV
BM 6061	9	− 713	32	270
HAZ 6061	8.5	− 713	34	244
MZ 4043	16	− 698	22	316

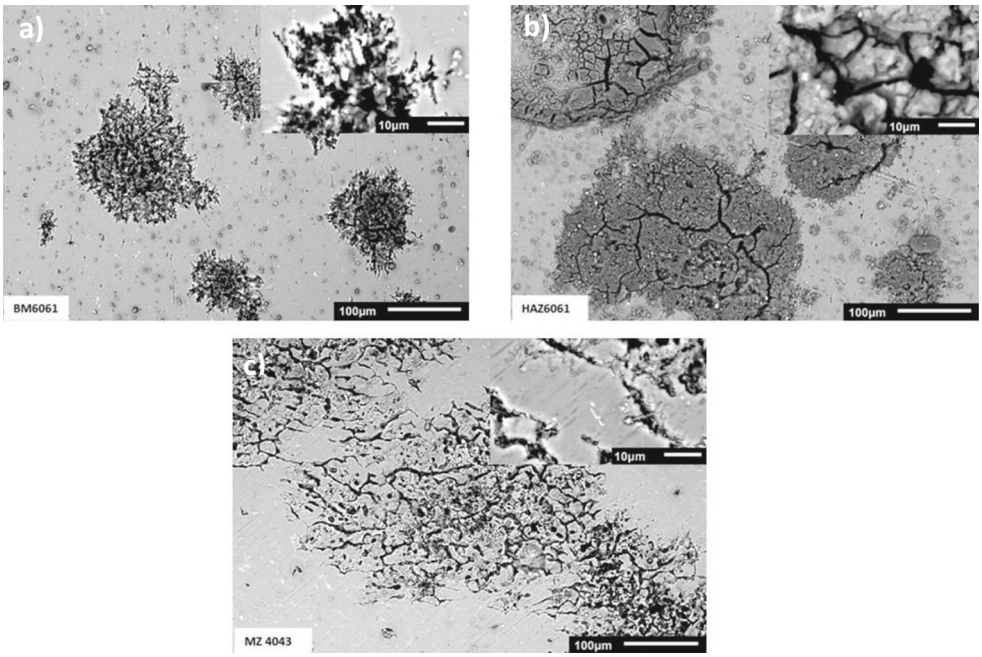

Fig. 13 Scanning electron micrographs of the corroded surfaces after anodic polarization of **a** BM, **b** HAZ, and **c** MZ

- A decrease in hardness of about 40% from BM to HAZ with 13% increase in absorbed energy are obtained. This is due to the microstructural changes and the presence of coalescent precipitates.
- Comparing the absorbed energy for each zone at different temperatures, no remarkable variation is noticed.
- Despite the slight increase in dimples size in the HAZ, the precipitates dispersion throughout the Al matrix and at the grain boundaries may explain the highest-absorbed energy already recorded there.
- The MZ exhibits the highest corrosion current density where the parameters resulted for BM and HAZ were relatively similar.

References

1. Mrowka-Nowotnic G, Sieniawski J (2005) Influence of heat treatment on the microstructure and mechanical properties of 6005 and 6082 aluminium alloys. J Mater Process Technol 162–163:367–372. https://doi.org/10.1016/j.jmatprotec.2005.02.115
2. Ozturk F, Sisman A, Toros S, Kilic S, Picu RC (2010) Influence of aging treatment on mechanical properties of 6061 aluminum alloy. Mater Des 31:972–975. https://doi.org/10.1016/j.matdes.2009.08.017
3. Wang L, Jin L, Huang W, Xu M, Xue J (2015) Effect of thermal frequency on AA6061 aluminum alloy double pulsed gas metal arc welding. Mater Manuf Process 31:2152–2157. https://doi.org/10.1080/10426914.2015.1103863
4. Martukanitz RP (1993) Selection and weldability of heat-treatable aluminum alloys. In: ASM handbook. Welding Brazing and Soldering, vol 6
5. Kumar TS, Balasubramanian V, Sanavullah MY (2007) Influences of pulsed current tungsten inert gas welding parameters on the tensile properties of AA 6061 aluminium alloy. Mater Des 28:2080–2092. https://doi.org/10.1016/j.matdes.2006.05.027
6. M K WHK (1987) Investigation of heat-affected zone cracking of GTA welds of Al-Mg-Si alloys using the Varestraint test. Weld J 66:360–368
7. Dwivedi D (2002) Influence of modifier and grain refiner on solidification behavior and mechanical properties of cast Al-Si base alloy. Inst Eng India 83:46–50
8. Lee WB, Yeon YM, Jung SB (2003) Evaluation of the microstructure and mechanical properties of friction stir welded 6005 aluminum alloy. Mater Sci Technol 19:1513–1518. https://doi.org/10.1179/026708303225008068
9. Simar A, Br Y, De MB et al (2008) Microstructure, local and global mechanical properties of friction stir welds in aluminium alloy 6005A-T6. Mater Sci Eng A 486:85–95. https://doi.org/10.1016/j.msea.2007.08.041
10. Heinz B, Skrotzki B (2002) Characterization of a friction-stir-welded aluminum alloy 6013. Metall Mater Trans B Process Metall Mater Process Sci 33B:489–498
11. Mathivanan A, Devakumaran K, Kumar AS (2014) Comparative study on mechanical and metallurgical properties of AA6061 aluminum alloy sheet weld by pulsed current and dual pulse gas metal arc welding arc welding processes. Mater Manuf Process 29:941–947. https://doi.org/10.1080/10426914.2014.912314
12. Narsimhachary D, Bathe RN, Padmanabham G, Basu A (2014) Influence of temperature profile during laser welding of aluminum alloy 6061 T6 on microstructure and mechanical properties. Mater Manuf Process 29:948–953. https://doi.org/10.1080/10426914.2013.872258
13. Elangovan K, Balasubramanian V (2008) Influences of tool pin profile and tool shoulder diameter on the formation of friction stir processing zone in AA6061 aluminium alloy. Mater Des 29:362–373. https://doi.org/10.1016/j.matdes.2007.01.030
14. Lakshminarayanan AK, Balasubramanian V, Elangovan K (2009) Effect of welding processes on tensile properties of AA6061 aluminium alloy joints. Inter J Adv Manuf Technol 40:286–296. https://doi.org/10.1007/s00170-007-1325-0
15. Dawood HI, Mohammed KS, Rahmat A, Uday MB (2015) Effect of small tool pin profiles on microstructures and mechanical

properties of 6061 aluminum alloy by friction stir welding. Trans Nonferrous Met Soc China 25:2856–2865. https://doi.org/10.1016/S1003-6326(15)63911-5
16. Wahid MA, Khan ZA, Siddiquee AN (2018) Review on underwater friction stir welding: a variant of friction stir welding with great potential of improving joint properties. Trans Nonferrous Met Soc China 28:193–219. https://doi.org/10.1016/S1003-6326(18)64653-9
17. Munoz AC, Ruckert G, Huneau B et al (2008) Comparison of TIG welded and friction stir welded Al-4.5Mg-0.26Sc alloy. J Mater Process Technol 197:337–343. https://doi.org/10.1016/j.jmatprotec.2007.06.035
18. Maisonnette D, Suery M, Nelias D, Chaudet P, Epicier T (2011) Effects of heat treatments on the microstructure and mechanical properties of a 6061 aluminium alloy. Mater Sci Eng A 528:2718–2724. https://doi.org/10.1016/j.msea.2010.12.011
19. Cicolin D, Trueba M, Trasatti SP (2014) Electrochim Acta Effect of chloride concentration, pH and dissolved oxygen, on the repassivation of 6082-T6 Al alloy. Electrochimi Acta 124:27–35. https://doi.org/10.1016/j.electacta.2013.09.003
20. Gharavi F, Matori KA, Yunus R, Othman NK, Fadaeifard F (2015) Corrosion behavior of Al6061 alloy weldment produced by friction stir welding process. J Mater Res Technol 4:314–322. https://doi.org/10.1016/j.jmrt.2015.01.007
21. ASME (2007) IX: Qualification Standard for Welding and Brazing Procedures, Welders, Brazers, and Welding and Brazing Operators, ASME International, The American Society of Mechanical Engineers (ASME), New York, United States
22. ASTM (2003) Standard Test Methods for Notched Bar Impact Testing of Metallic Materials (Designation: E23), ASTM International, West Conshohocken, United States
23. Andersen SJ, Zandbergen HW, Jansen J, TrÆholt C, Tundal U, Reiso O (1998) The crystal structure of the b phase in Al-mg-Si alloys. Acta Mater 46:3283–3298
24. Massardier V, Epicier T (2002) Study of the influence of a low copper addition and of an excess of silicon on the precipitation kinetics and on the precipitation sequence of Al-Mg2Si alloys. Mater Sci Forum 402:851–856. https://doi.org/10.4028/www.scientific.net/MSF.396-402.851.
25. Murayama M, Hono K (1999) Pre-precipitate clusters and precipitation processes in Al-Mg-Si alloys. Acta Mater 47:1537–1548. https://doi.org/10.1016/S1359-6454(99)00033-6
26. Fang X, Song M, Li K, Du Y (2010) Precipitation sequence of an aged Al-Mg-Si alloy. J Min Metall Sect B: Metall 46:171–180. https://doi.org/10.2298/JMMB1002171F
27. Menzemer C, Lam PC, Srivatsan TS, Wittel CF (1999) Investigation of fusion zone microstructures of welded aluminum alloy joints. Mater Lett 41:192–197. https://doi.org/10.1016/S0167-577X(99)00129-9.
28. JIA Z, DING L, WENG Y et al (2016) Effect of high temperature pre-straining on the natural aging and bake hardening response of Al-Mg-Si alloys. Trans Nonferrous Met Soc China 26:924–929. https://doi.org/10.1016/j.jallcom.2016.07.066.
29. Devaraj A, Perea DE, Liu J, Gordon LM, Prosa TJ, Parikh P, Diercks DR, Meher S, Kolli RP, Meng YS, Thevuthasan S (2017) Three-dimensional nanoscale characterisation of materials by atom probe tomography. Int Mater Rev 63:68–101. https://doi.org/10.1080/09506608.2016.1270728
30. Yang X, Liu J, Chen J, Wan C, Fang L, Liu P, Wu C (2014) Relationship between the strengthening effect and the. Acta Metall Sin (Engl Lett) 27:1070–1077. https://doi.org/10.1007/s40195-014-0122-7
31. Starke EA Jr (1977) Aluminium alloys of the 70's: scientific solutions to engineering problems. An invited review. Mater Sci Eng 29:99–115. https://doi.org/10.1016/0025-5416(77)90114-8
32. Wang HQ, Sun WL, Xing YQ (2013) Microstructure analysis on 6061 aluminum alloy after casting and diffuses annealing process. Phys Procedia 50:68–75. https://doi.org/10.1016/j.phpro.2013.11.013
33. Zhang Z, Xu H, Wu S, Liu Y (2013) Effects of combined pre-straining and pre-aging on natural aging and bakehardening response of an Al-Mg-Si alloy. Acta Metall Sin (Engl Lett) 26:340–344. https://doi.org/10.1007/s40195-012-0239-5
34. Losana L (1931) The ternary system Al-Mg-Si (in Italian) (Equi. Diagram, experimental, 14). Met Ital 23:367–382
35. Milkereit B, Wanderka N, Schick C, Kessler O (2012) Continuous cooling precipitation diagrams of Al-Mg-Si alloys. Mater Sci Eng A 550:87–96. https://doi.org/10.1016/j.msea.2012.04.033
36. Lin DC, Wang GX, Srivatsan TS (2003) A mechanism for the formation of equiaxed grains in welds of aluminum Á lithium alloy 2090. Technical note Mater Sci Eng A 351:304–309. https://doi.org/10.1016/S0921-5093(02)00858-4
37. Ahmad R, Asmael MBA (2016) Influence of cerium on microstructure and solidification of eutectic Al-Si piston alloy. Mater Manuf Process 31:1948–1957. https://doi.org/10.1080/10426914.2015.1127942
38. Madhusudhan Reddy G, Gokhale AA, Prasad Rao K (1997) Weld microstructure refinement in a 1441 grade aluminium-lithium alloy. J Mater Sci 32:4117–4126
39. Abúndez A, Pereyra I, Campillo B, Serna S, Alcudia E, Molina A, Blanco A, Mayén J (2016) Improvement of ultimate tensile strength by artificial ageing and retrogression treatment of aluminium alloy 6061. Mater Sci Eng A 668:201–207. https://doi.org/10.1016/j.msea.2016.05.062
40. Feufel H, Gödecke T, Lukas HL, Sommer F (1997) Investigation of the Al-Mg-Si system by experiments and thermodynamic calculations. J Alloys Compd 247:31–42. https://doi.org/10.1016/S0925-8388(96)02655-2
41. Reiso O, Ryum N, Strid J (1993) Melting of secondary phase particles in Al-Mg-Si alloys. Met Mater Trans A 24:2629–2641
42. Manti R, Dwivedi DK, Agarwal A (2008) Microstructure and hardness of Al-Mg-Si weldments produced by pulse GTA welding. Int J Adv Manuf Technol 36:263–269. https://doi.org/10.1007/s00170-006-0849-z
43. Kumar V, Singh IV, Mishra BK, Jayaganthan R (2014) Improved fracture toughness of cryorolled and room temperature rolled 6082 al alloys. Acta Met Sin (Engl Lett) 27:359–367. https://doi.org/10.1007/s40195-014-0057-z